KeAi
CHINESE ROOTS
GLOBAL IMPACT

Available online at www.keaipublishing.com/en/journals/journal-of-magnesium-and-alloys/

ScienceDirect

Journal of Magnesium and Alloys 12 (2024) 4709–4721

www.elsevier.com/locate/jma

Full Length Article

Strength–ductility synergy in Mg-Gd-Y-Zr alloys via texture engineering in bi-directional forging

Jingli Li[a,b,1,*], Quanfeng Han[b,1], Xiuzhu Han[a,c], Xin Yi[b,*]

[a] *Institute for Advanced Materials, North China Electric Power University, Beijing 102206, China*
[b] *Department of Mechanics and Engineering Science, College of Engineering, Peking University, Beijing 100871, China*
[c] *Beijing Institute of Spacecraft System Engineering, Beijing 100094, China*

Received 9 May 2023; received in revised form 19 December 2023; accepted 25 December 2023
Available online 20 January 2024

Abstract

In this work, we successfully fabricate an ultra-high strength Mg-11Gd-3Y-0.5Zr alloy with ultimate tensile strength of 523 MPa and enhanced ductility via cost-effective bi-directional forging (BDF) and subsequent annealing heat treatments. To elucidate the role of BDF and gain a fundamental understanding of the remarkable simultaneous increase of strength and ductility, systematic microstructure characterization and analysis are performed. It is revealed that the double-peak basal texture, with basal poles located at the center of two mutually perpendicular forging directions, serves as an essential factor for the strength–ductility synergy of the Mg-11Gd-3Y-0.5Zr alloy processed with BDF. Roles of the double-peak basal texture in overcoming the strength–ductility trade-off include promoting non-basal slip, increasing ductility, and enlarging the Hall–Petch effect along the sample elongation direction while reducing the extent of anisotropy in critical resolved shear stresses of different slip systems. This study demonstrates that texture engineering is a powerful strategy to control magnesium alloy performance and BDF is a promising processing technique for enhancing mechanical properties of magnesium alloys.

Keywords: Bi-directional forging (BDF); Magnesium alloys; High strength; Texture; Anisotropy.

1. Introduction

Magnesium (Mg) has the highest strength-to-weight ratio among all structural metals, but its low intrinsic strength and ductility as well as high susceptibility to cracking caused by hexagonal close-packed (HCP) crystal structure limits its broad engineering applications as structural components. Developing Mg alloys with both high strength and high formability is highly desired. As Mg alloys exhibit a remarkable fine-grain strengthening effect [1], a promising way for improving mechanical properties of Mg alloys is grain refinement using severe plastic deformation (SPD) techniques [2–5]. Various SPD techniques, such as equal channel angular pressing (ECAP) [2], cyclic extrusion compression (CEC) [3,4] and multi-directional forging (MDF) processes [5], are known for greatly refining the microstructure of Mg alloys to submicron or even nanoscale dimensions. Nevertheless, the effect of SPD processes on mechanical properties of Mg alloys is complex. While grain refinement strengthens Mg alloys, the texture modification during SPD with rotation of basal planes towards the orientation for easier slip could lead to a reduction in yield strength, a phenomenon known as texture softening [6–8]. Therefore, the yield strength of Mg alloys with SPD can be recognized as a result of competition between the strengthening effect from grain refinement and the texture softening effect depending on texture type and intensity [8–10]. Owing to a much lower texture intensity associated with the addition of rare earth (RE) elements to Mg alloys, the grain size strengthening effect of Mg-RE alloys upon SPD is significant [2,9,10]. For instance,

* Corresponding authors.
E-mail addresses: lijingli@ncepu.edu.cn (J. Li), xyi@pku.edu.cn (X. Yi).
[1] J.L. and Q.H. contributed equally to this work.

https://doi.org/10.1016/j.jma.2023.12.013

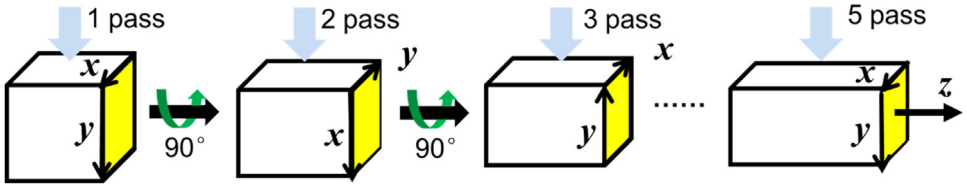

Fig. 1. Schematic of the bi-directional forging (BDF) process. *x*, *y*, and *z* coordinates are along the block edges. Forging direction is perpendicular to the *xz* plane. The $x \times y$ dimensions of the block before and after the BDF process is 60 mm × 60 mm and 32 mm × 35 mm, respectively.

Mg-8Gd-3Y-1Zn (in weight percent, wt.%) alloys with a high yield strength of up to 456 MPa can be fabricated via hot extrusion, ECAP, and subsequent aging treatment [11].

Polycrystalline alloys often show a strength-ductility paradox, a phenomenon in which increasing the material strength leads to a decrease in ductility [12]. Due to the strength–ductility trade-off, only a few Mg alloys processed through SPD are reported to exhibit a simultaneous increase in strength and ductility, and the toughening mechanism varies across different alloys. For instance, it is reported that non-basal slip in fine-grained Mg alloys might be responsible for the high ductility of Mg-9.8Gd-1.6Y-0.02Zn-0.5Zr (GW102, wt.%) alloys processed through CEC [3]. Tong et al. attributed the improved ductility of Mg-8.2Gd-3.8Y-1Zn-0.4Zr (wt.%) alloys processed at a decreased temperature using MDF to the breaking of coarse long-period stacking ordered phases into small pieces [10]. Except to these few case studies, there is a lack of systematic investigation on revealing the plastic deformation mechanism related to the enhanced ductility in high-strength alloys processed using SPD techniques.

The MDF process is an effective and costly technique used in industries for grain refinement, but few reports exist on ultra-high-strength Mg-RE alloys processed using MDF [13,14]. In this work, a new forging process, which we call bi-directional forging (BDF), is proposed and successfully applied to fabricate high-performance Mg-Gd-Y-Zr alloys of improved yield strength and elongation. Upon further treatment, ultra-high strength is achieved. Microstructure and mechanical behaviors of Mg-Gd-Y-Zr alloys processed using BDF are analyzed to reveal the strengthening and toughening mechanisms as well as texture effect on mechanical properties of Mg-RE alloys. Our results demonstrate the powerful capability of BDF in processing high-performance Mg-RE alloys and provide mechanistic guides to design of magnesium alloys.

2. Materials and experimental procedure

The Mg-11.0Gd-3.0Y-0.5Zr (wt.%) alloy used in this study, referred to as GW113, is manufactured using permeant mold casting. To reduce casting defects, the cast ingot is subjected to hot isostatic pressing at 480°C and 100 MPa for 3 hours. Blocks with dimensions 60 mm × 60 mm × 60 mm are cut from the GW113 ingot and then undergo the homogenization process (solution heat treatment at 525 °C for 12 hours, followed by air cooling). Some of the blocks are directly used for mechanical testing in the as-homogenized state, and rest blocks are further forged. Forging is performed at 450°C before which these blocks are heated for 30 minutes in a resistance furnace. Fig. 1 shows a schematic of the BDF process. A conventional industrial air-pneumatic hammer with a load gravity of 750 kg is used for forging with the block rotated 90° around the *z*-axis after each pass. A total of five forging passes result in a total strain of 1.83 along the elongation direction (ED) or *z*-direction in Fig. 1. The block processed with BDF cools down gradually in room temperature air. No cracks are observed in the GW113 alloys processed using BDF. For simplicity, alloys processed using BDF are referred to as BDFed alloys hereinafter. A representative image of the BDFed GW113 alloy is shown in Fig. 2.

Uniaxial tensile experiments on the PFD and PED samples (Fig. 2) cut from the forged blocks are performed using an electronic type universal testing machine at room temperature with a strain rate of 1×10^{-3} s^{-1}, and for each tensile condition the tests are repeated three times. The dog-bone shaped tensile specimens have gauge dimensions of 10 mm × 2.5 mm × 3 mm.

Optical microscopy (OM), scanning electron microscope (SEM), and transmission electron microscope (TEM) are used for microstructural observations of the BDFed samples. An energy dispersive spectrometer (EDS) is used to perform a semi-quantitative compositional analysis of the second phase in the GW113 alloy. X-ray diffraction (XRD) is used to measure the macrotexture of the BDFed samples. The specimens for OM are prepared by grounding and mechanical polishing, followed by etching in acetic-picric acid solution (25 mL ethanol + 2 g picric acid + 5 mL acetic acid + 5 mL distilled water). Electron back-scattered diffraction (EBSD) measurements are carried out for orientation analysis using a JEOL-JSM-7001F field emission SEM equipped with an automated orientation acquisition system (Oxford Instruments HKL Chanel 5). For EBSD observation, the specimens are prepared by electropolishing. The EBSD scanning step size here is 1.5 μm. Thin foil samples for TEM are prepared

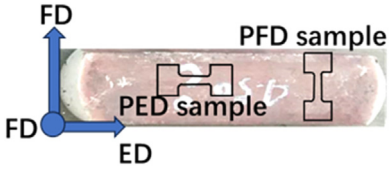

Fig. 2. A forged block marked with locations of two tensile samples. The PFD and PED samples refer to tensile samples with axial directions parallel to the forging direction (FD) and elongation direction (ED), respectively.

by punching discs of 3 mm diameter, followed by dimple grinding and Ar ion milling in a precision ion polishing system (Leica EM RES101).

The plastic deformation mechanism of the BDFed alloy under tension is analyzed in detail by examining the activation of slip systems and characterizing the intergranular strain coordination. The slip system activation of the Mg-RE alloy could be revealed by quasi-in-situ EBSD experiments before and after stretching on selected regions. Using the slip trace method [15], active slip systems associated with the real slip traces detected using SEM are identified by comparing observed slip traces with theoretical slip traces predicted using MTEX, a free MATLAB toolbox for analyzing the influence of crystallographic textures. STABiX software [16] is used to determine the strain coordination factor $m' = \cos\psi \times \cos\kappa$, where ψ is the angle between the plane normal vectors of two involved slip systems and κ is the angle between the Burgers vectors [17].

3. Results

3.1. Microstructure

OM and SEM images of the GW113 alloy in the as-homogenized state are presented in Fig. 3. One can see that the alloy in the as-homogenized state consists of equiaxed coarse grains with an average grain size of 92.5 μm. A small amount of insoluble second phase particles (black dots and small white squares in Fig. 3a,b) present in the homogeneous α-Mg solid solution are randomly distributed within grains and at grain boundaries (GBs). Using secondary ion mass spectrometry and other characterization methods, these particles were determined as the RE-hydride [18], which is difficult to eliminate through heat treatments. The RE-hydride distribution under different solid solution and aging heat treatments indicates that the volume fraction of the RE-hydride is generally less than 1%. Here we ignore the strengthening and toughening contributions from the RE-hydride.

Figs. 4-7 show the microstructure of the BDFed GW113 alloy at different length scales. The OM images in Fig. 4 show that the sample processed by BDF exhibits microstructure consisting of fine grains, coarse grains, and twins, with no apparent anisotropy. Both the fine dynamic recrystallized (DRX) grains and coarse grains have equiaxed shapes and are significantly smaller than the initial grains shown in

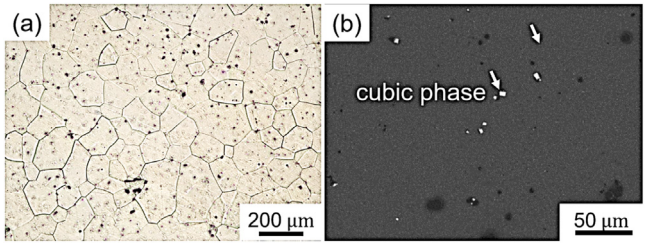

Fig. 3. (a) Initial OM and (b) SEM images of the GW113 alloy in the as-homogenized state.

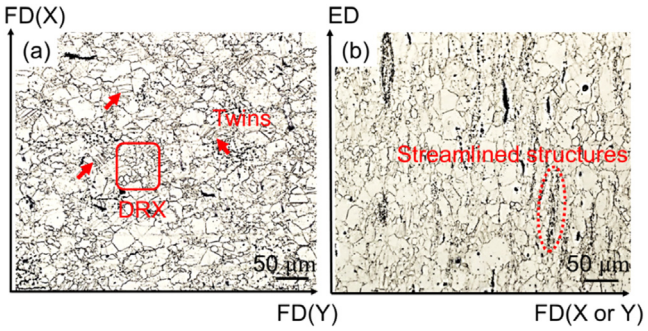

Fig. 4. OM images of the BDFed sample observed along elongation direction (ED) (a) and forging direction (FD) (b). Arrows in (a) label twins.

Fig. 3a. In addition, Fig. 4b shows streamlined structures in the sample along the ED direction, which appear as black dots when viewed from the FD direction. The EDS results from TEM analysis reveal that the RE-rich phases contribute to these streamlined structures due to the segregation of RE elements during solidification or processing. Fig. 5a,b shows that some of the RE-rich phases in the streamlined structures contain elements such as Mn, Cr, and Ni that are not included in the alloy composition, suggesting the possibility of adsorption of impurities by the RE elements during casting. In contrast, Fig. 5c indicates that only RE elements are detected in the coarse and white squares in the streamlined structures. The white squares may consist of RE-hydrides, which are known to be difficult to detect using EDS due to the low hydrogen content and the small size of the hydride particles. The casting defects and RE-hydrides in the initial microstructure might be redistributed during the BDF process due to the complex stress flow, leading to a streamlined distribution pattern. These RE-rich phases may promote recrystallization via particle-stimulated nucleation and hinder grain growth, resulting in the formation of fine grains in the streamlined structures. Furthermore, dense nanoprecipitates exist in the BDFed sample (Fig. 5d), which were probably formed during forging and air cooling. The selected area electron diffraction (SAED) patterns in Fig. 5e,f suggest that these nanoprecipitates are a combination of β′ and β″ phases [19]. The plate-shaped precipitate phase β′, commonly found on the prismatic planes of magnesium, is the dominant strengthening phase in Mg-RE alloys that can significantly hinder the basal slip [20]. Therefore, the BDFed sample is expected to exhibit high strength. By performing an inverse fast Fourier transform (IFFT) analysis on the circular region in Fig. 5d along $[01\bar{1}0]$ direction, many dislocations in the BDFed sample were identified (Fig. 5g). Since the dynamic recrystallization process consumes dislocations and releases residual stress, work hardening shall not be the dominant strengthening mechanism in the BDFed sample.

Fig. 6a shows an inverse pole figure (IPF) map of the BDFed sample. The microstructure consists of fine and relatively coarse grains decorated with plentiful twins, suggesting a bimodal grain size distribution though the distribution of relatively coarse grains is very scattered. Excluding and

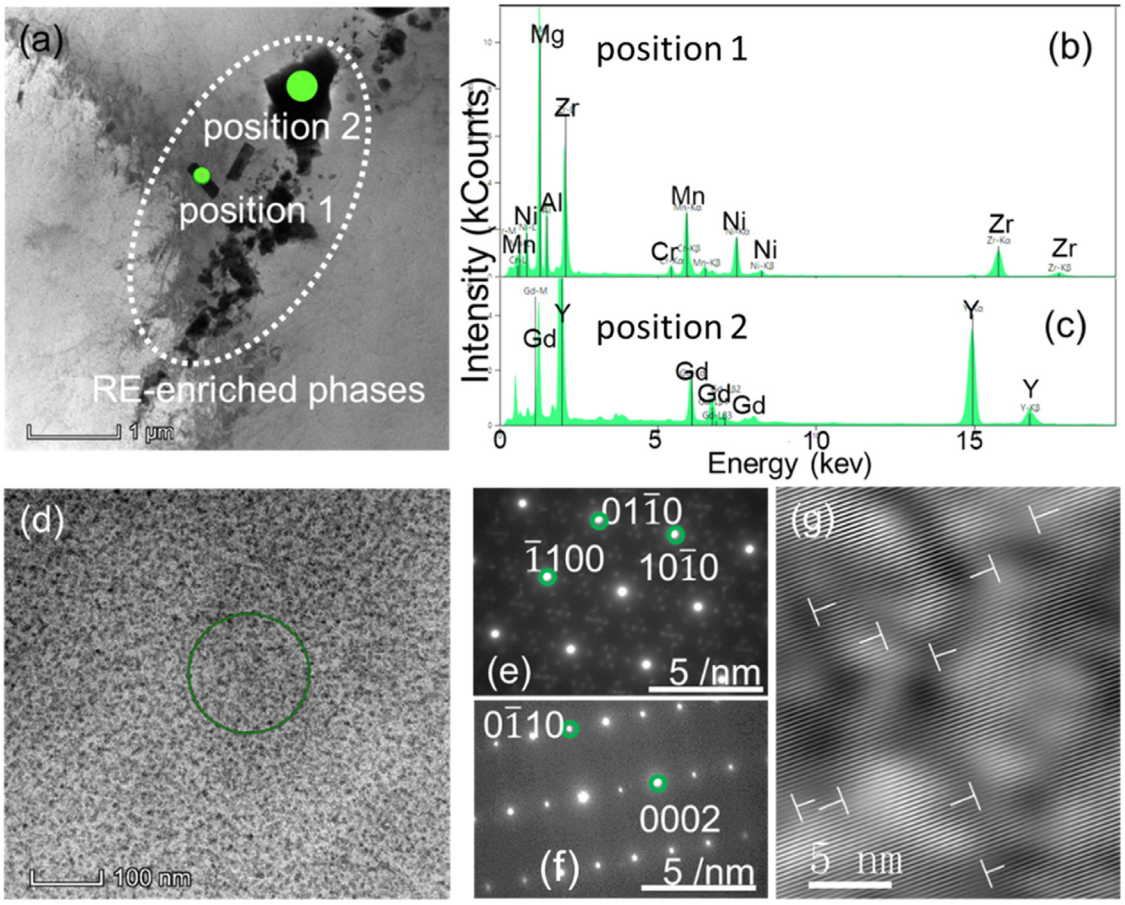

Fig. 5. TEM images showing precipitates in the BDFed sample. The bright field image of the streamlined structures (a) and EDS spectra of positions 1 and 2 (b,c). The bright field image of the nanoprecipitates (d) and the corresponding diffraction pattern with an incident beam along [0001] (e) and [11$\bar{2}$0] directions (f). (g) IFFT analysis on the circular region in (d) revealing dislocations in the BDFed sample.

including twin boundaries (TBs), the average grain sizes are about 11.7 μm and 10.7 μm (Fig. 6b), respectively, much smaller than that of the sample in the as-homogenized state (92.5 μm). Abundant {10$\bar{1}$2} twins were observed in the BDFed Mg-RE alloys (Fig. 6c), leading to a GB misorientation distribution peak at 80°–90° with a misorientation axis of <$\bar{1}2\bar{1}0$> (Fig. 6d). The proportion of low angle GBs, which can hinder dislocation movement and dissipate energy under high stress [21], is as high as 67.8%.

The texture of the BDFed GW113 alloys was analyzed using EBSD and XRD (Fig. 7). The basal texture with <01$\bar{1}$0> direction parallel to ED has a double-peak distribution. The two peaks are titled around 39° from FD (x) to FD (y). This type of texture was observed in Ca-containing and RE-containing Mg-Zn alloys [22,23], which improves the formability and cold workability of the alloys.

3.2. Mechanical properties

Fig. 8a displays stress-strain curves of the as-homogenized sample and BDFed samples cut along ED and FD (PED and PFD), and Fig. 8b shows the corresponding mechanical property histogram. The BDF process significantly enhanced the strength and ductility of the GW113 alloy, with the PED sample exhibiting a yield strength and elongation of 312 MPa and 14.5%, respectively. However, mechanical properties of the PFD sample remain almost unchanged in comparison with the sample in the as-homogenized state, indicating significant anisotropy. Ratios of the ultimate tensile strength (UTS), 0.2% offset yield strength (YS), and elongation (EL) between the PED and PFD samples are 1.62, 2.27, and 3.45, respectively. It is intriguing that the BDF process resulted in increased strength and ductility along ED but almost no effect along FD.

The influence of annealing treatments at 225 °C and 250 °C on the mechanical properties of the BDFed GW113 samples was examined. The duration of the treatments was chosen in accordance with peak-aging parameters for Mg-RE alloys, such as GW103 and GW94, with the objective of maximizing precipitation strengthening [24,25]. Table 1 presents the mechanical properties of both the BDFed GW113 alloys and the cast GW113 alloy (in its as-homogenized state) following annealing treatment at 250 °C and 225 °C. It is indicated that the annealing treatments at 225 °C to 250 °C improved the strength but decreased the ductility of both cast and BDFed alloys in both ED (PED sample) and FD (PFD sample). The anisotropy of the BDFed alloys in ED

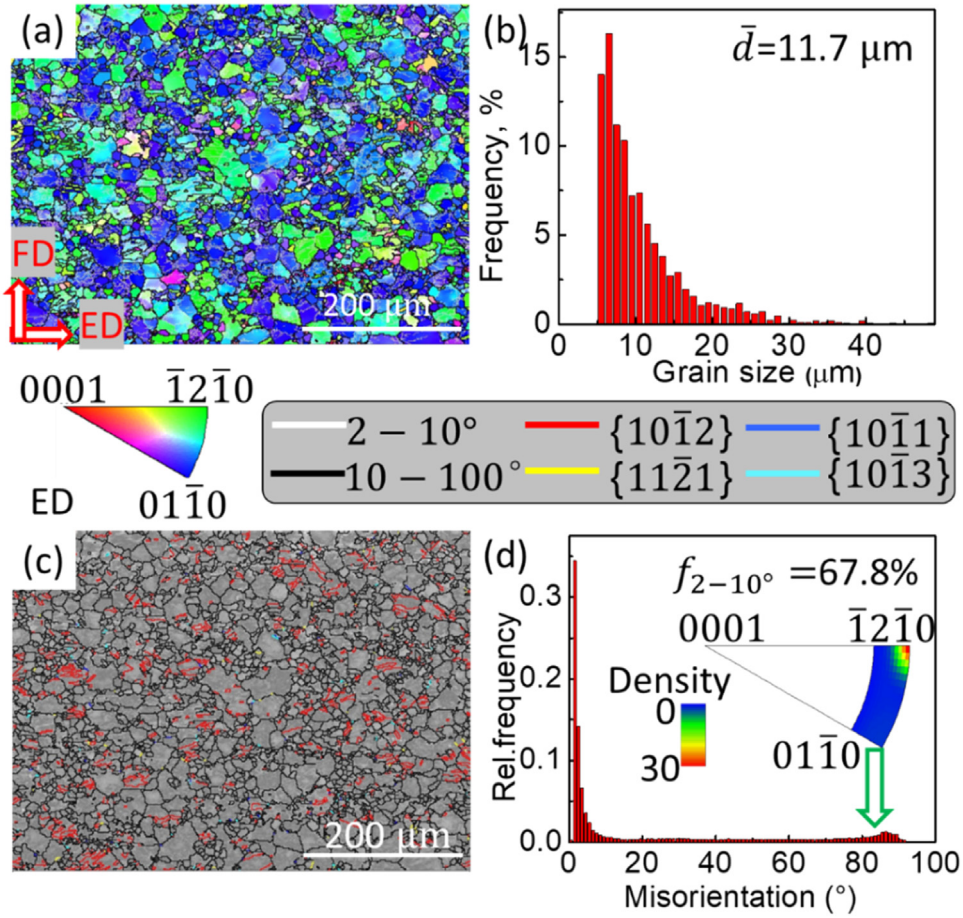

Fig. 6. The EBSD results of the BDFed sample. IPF colored map (a), grain size distribution (b), image quality (IQ) figure with GBs and TBs (c), and GB misorientation distribution (d). Black, white, red, yellow, blue and cyan lines represent high angle GBs, low angle GBs, {10$\bar{1}$2} TBs, {11$\bar{2}$1} TBs, {10$\bar{1}$1} TBs and {10$\bar{1}$3} TBs, respectively.

Table 1
Mechanical properties of the GW113 alloys in as-homogenized and BDFed conditions, subjected to various annealing treatments.

Alloys	Heat treatment	Ultimate tensile strength (MPa)	Yield strength (MPa, 0.2% offset)	Elongation (%)
Cast GW113	Homogenization + 250°C × 12 h	331	249	0.76
BDFed GW113	PED + 250°C × 12 h	464^{+4}_{-3}	405^{+5}_{-4}	$5^{+2.03}_{-1.86}$
	PFD + 250°C × 12 h	273^{+17}_{-19}	188^{+43}_{-27}	$0.8^{+0.12}_{-0.16}$
	PED + 225°C × 32 h	$516^{+7.1}_{-12}$ (523.1, maximum)	$474^{+6}_{-6.7}$ (480, maximum)	$2.42^{+1.26}_{-0.68}$ (3.68, maximum)

and FD remains unchanged upon the annealing treatments at 225 °C and 250 °C. Among the selected annealing treatment conditions in Table 1, 225 °C for 32 hours is optimal for the BDFed samples, resulting in the maximum ultimate tensile strength, 0.2% offset yield strength, and elongation of the PED tensile sample as 523.1 MPa, 480 MPa, and 3.68%, respectively.

As shown in Fig. 9, the 0.2% offset yield strength of the PED sample after the annealing treatment at 225 °C × 32 h is higher than that of most magnesium alloys obtained by a single processing method (such as extrusion, rolling, forging, and MDF) and aging treatment, as reported in refs. [26–31] and presented in green elliptical area in Fig. 9. It is worth mentioning that there have been limited studies on utilizing SPD techniques, such as ECAP and HPT (hot pressure torsion), directly on cast Mg-RE alloys, with the exception of MDF. Excitingly, the highest yield strength and ductility of the BDFed GW113 alloy with the annealing treatments at 225 °C to 250 °C can be comparable to those of magnesium alloys obtained by combining multiple processing methods (such as extrusion + rolling and extrusion + ECAP) and aging treatments [32–36], as shown in the yellow elliptical area. In comparison with GW94 and EW75 alloys processed with MDF (marked in the blue area), the BDFed GW113 exhibits significantly higher strength and ductility, indicating that the BDF process is more effective than the often-used triaxial MDF process in enhancing mechanical properties of Mg-RE alloys with similar compositions. Moreover, mechan-

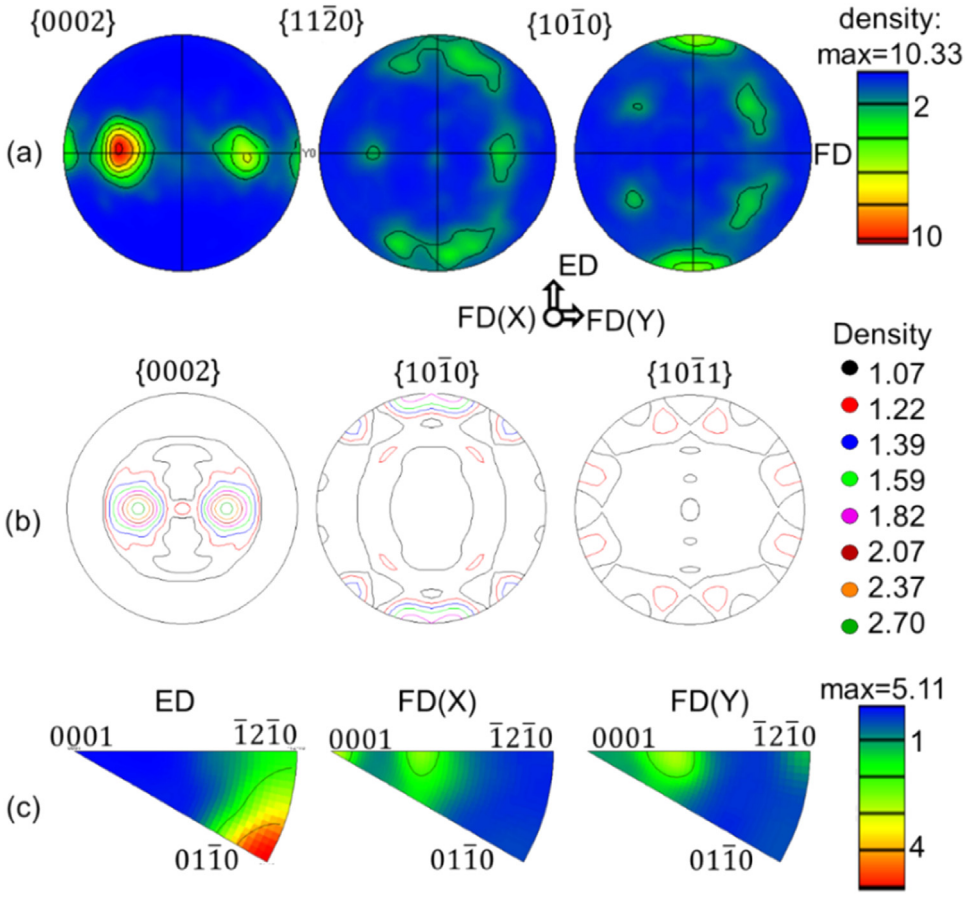

Fig. 7. Pole figures (a,b) and IPF (c) of the BDFed sample characterized by EBSD (a,c) and XRD (b).

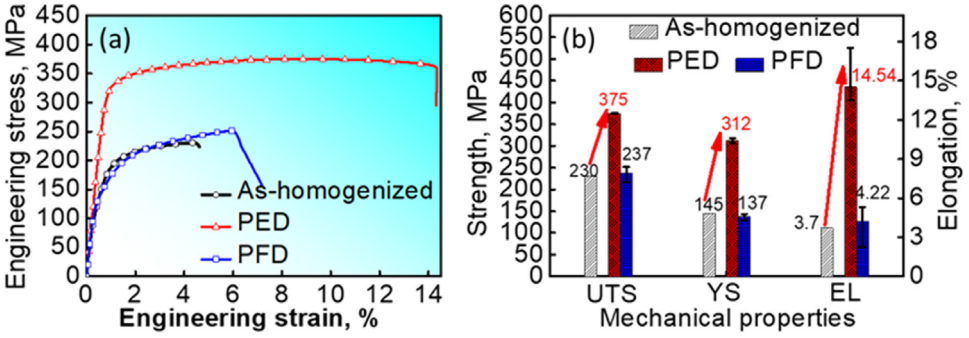

Fig. 8. (a) Engineering stress-engineering strain curves and (b) mechanical properties of the GW113 alloy in the initial as-homogenized state and BDFed state (PED and PFD samples).

ical properties of GW113 processed with BDF but without the annealing treatments at 225 °C to 250 °C are comparable to those of many Mg-RE alloys upon hot working and aging or annealing treatment (in the gray area). Therefore, BDF, requiring fewer processes and following treatments, is a cost-effective and energy-saving process for producing magnesium alloys with improved mechanical properties.

Morphologies of fracture surfaces of the PED and PFD samples are shown in Fig. 10a-c and d-f, respectively, both exhibiting a quasi-cleavage fracture feature with the presence of dimples and cleavage planes. The streamlined structure formed during BDF could be observed on the fracture surface of the PFD sample (Fig. 10e) but not on the fracture surface of the PED sample (Fig. 10b), suggesting that the streamlined structure could initiate cracks and deteriorate ductility. However, Fig. 10c,f demonstrates that precipitates in the streamlined structure are located at the base of the dimples, indicating that plastic deformation responds to the stress concentration at the precipitates. Therefore, the streamlined structure may not be the primary factor causing a significant lower ductility of the PFD sample in comparison with that of the PED sample.

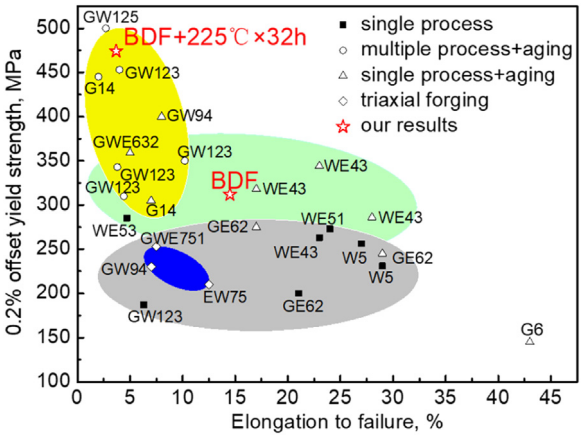

Fig. 9. Mechanical properties of high-strength Mg-RE alloys upon different processes and heat treatments. Data are from refs. [12,13,26-36].

4. Discussion

The BDFed alloy improves strength and ductility when loaded along ED but remains unchanged along FD, suggesting that isotropic grain refinement (Fig. 4) is not the primary reason for the simultaneous improvement of strength and ductility in the PED sample. The underlying strengthening and toughness mechanism and anisotropic mechanism due to the BDF process need to be revealed to guide the processing technology of obtaining magnesium alloys with high strength and exceptional ductility.

4.1. Strengthening mechanism of the GW113 sample processed with BDF

The microstructure evolution during the BDF process (Figs. 3-7) indicates that the strengthening mechanisms of the high-strength GW113 alloys include precipitate strengthening, grain boundary strengthening, twin strengthening, and texture strengthening. While many existing studies attribute the main strengthening mechanism of high-strength Mg-RE alloys to precipitate strengthening and grain boundary strengthening [2,10], the current work emphasizes the crucial influence of texture due to the observation of anisotropic mechanical properties along ED and FD directions, despite isotropic precipitates and grains.

Fig. 11a-c shows the basal slip Schmid factor (m_{basal}) maps of the BDFed GW113 alloy when tension along ED and FD(x and y). The corresponding Schmid factor frequency in Fig. 11d indicates that most grains have low values of m_{basal} for the PED sample (<0.2), and the highest Schmid factor of basal slip for the preferred orientations in the PFD sample is larger than 0.4. The average Schmid factors of basal slip ($\bar{m}_{\mathrm{basal}}$) when loaded along ED and FD are $\bar{m}^{\mathrm{PED}}_{\mathrm{basal}} = 0.16$ and $\bar{m}^{\mathrm{PFD}}_{\mathrm{basal}} = 0.38$, respectively. Previous studies have demonstrated that grain orientation significantly affects the Hall–Petch effect as [5,37-39]

$$\sigma_{\mathrm{y}} = \sigma_0 + kd^{-1/2},$$

where σ_{y} is the yield stress, $\sigma_0 = \tau_{\mathrm{c}}/m$ with m indicating the Schmid factor is the friction stress when dislocation glide on the slip plane with τ_{c} as the critical resolved shear stress (CRSS), k coefficient constant, and d grain size. Therefore, the PED sample with $\bar{m}^{\mathrm{PED}}_{\mathrm{basal}}$ of a lower value experiences greater strengthening due to grain refinement compared to the PFD sample with $\bar{m}^{\mathrm{PFD}}_{\mathrm{basal}}$ of a higher value.

We now discuss the precipitate strengthening. The annealing treatments at 225 °C to 250 °C lead to the growth of β′ phase and the transition from β″ to β′ without changing the total volume fraction f of precipitates (around 12%, see Figs. 5d and 12a). This indicates that there were probably no

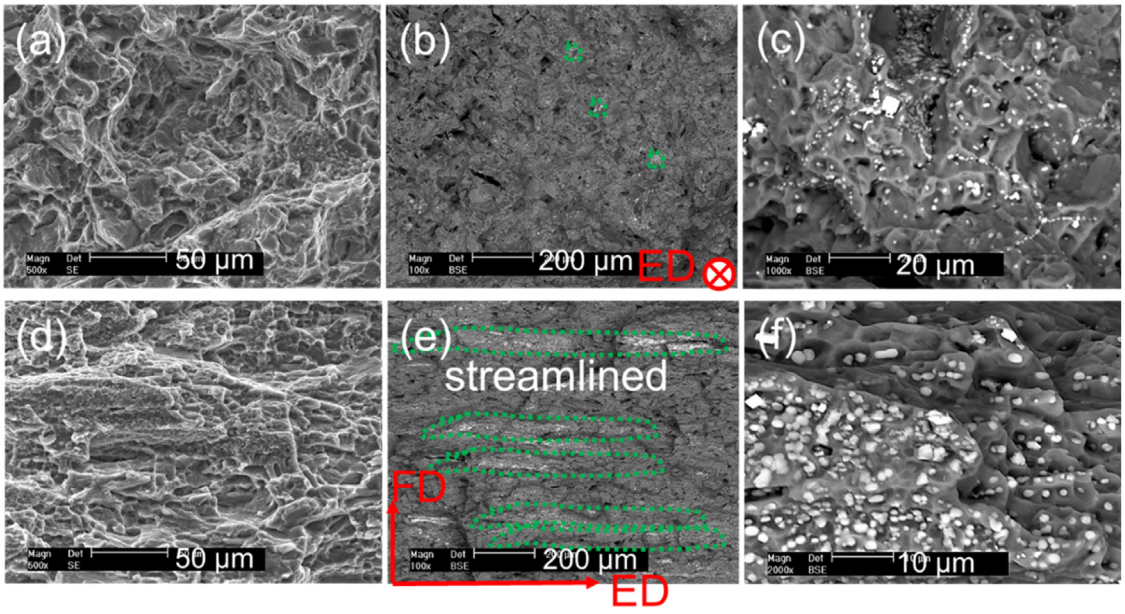

Fig. 10. Fracture morphologies of the PED (a-c) and PFD (d-f) samples in the second electron (SE) mode (a,d) and backscatter electrons (BSE) mode (b,c,e,f). (c,f) Magnified views of the streamlined structure.

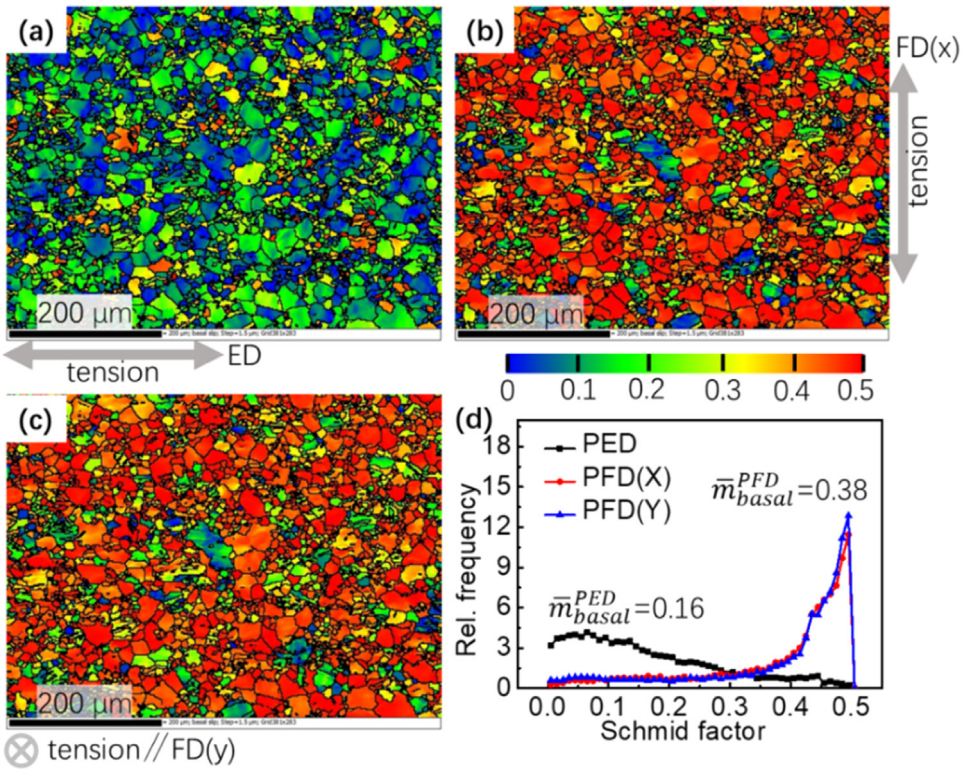

Fig. 11. (a-c) Distributions of basal slip Schmid factor (m_{basal}) of the BDFed GW113 alloy (Fig. 6) when loaded along ED (a), FD(x) (b), and FD(y) (c). (d) The m_{basal} distribution frequency under these three loading conditions.

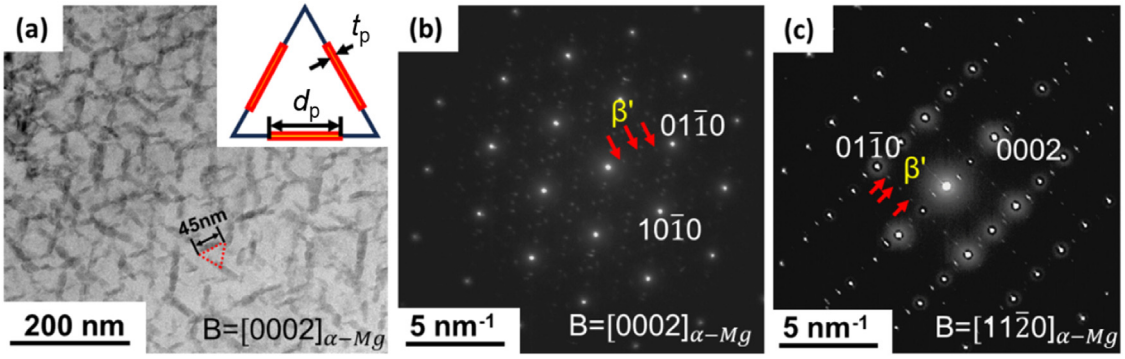

Fig. 12. (a) TEM images of precipitates in the BDFed sample after annealing treatment. The mean planar diameter is d_p = 45 nm and mean planar thickness is t_p = 10 nm in (0002) slip plane. The corresponding SAED pattern along the incident beam direction **B** = [0002] (b) and [11$\bar{2}$0] (c).

new precipitations occurring, but rather only aging precipitate evolution occurred. Fig. 5d,f shows that the maximum precipitate radius r_{max} is approximately 2.5 nm in the BDFed samples and Fig. 12a shows the mean planar diameter d_p in (0002) slip plane of α-Mg around 45 nm and the mean planar thickness t_p around 10 nm in the BDFed samples after the heat treatments. According to the Orowan mechanism suggesting that strength is proportional to the volume fraction and inversely proportional to the size of dispersed second phase [40], the BDFed samples with dense precipitation in Fig. 5d are supposed to exhibit a stronger strengthening effect in comparison with the BDF+250 °C × 12 h samples in Fig. 12a. However, this is not the case (Fig. 8 and Table 1). Therefore, we infer the dislocation cutting fine precipitates (including β″ and β′) in the BDFed samples, instead of dislocation bowing.

Depending on the size and dispersion of the precipitates, there are two main mechanisms for precipitation hardening, cutting mechanism associated with dislocation cutting fine precipitate particles and Orowan mechanism with dislocation bowing around larger precipitates [41–43]. Depending on the spacing of the dislocation pairs in comparison with the precipitate diameter, two situations of particle cutting, the case of weakly coupled dislocation pairs and the case of strongly coupled dislocation pairs, can be further distinguished. According to the classical precipitation-strengthening model [41–43], the shear stress required for cutting by the

weak-coupling mechanism is

$$\tau_{\text{weak}}^{\text{cutting}} = \frac{\gamma_{\text{APB}}}{2b}\left(\frac{1}{b}\sqrt{\frac{6\gamma_{\text{APB}} fr}{\pi G}} - f\right), \quad (1)$$

where γ_{APB} is the anti-phase boundary energy acting as a barrier which must be overcome for particle cutting to take place, b is the magnitude of the Burgers vector, f is the precipitate volume fraction, r is the precipitate radius, and G is the shear modulus of the matrix.

The CRSS for the case of strongly coupled dislocations cutting precipitates is

$$\tau_{\text{strong}}^{\text{cutting}} = \frac{Gb}{\pi r}\sqrt{\frac{3\gamma_{\text{APB}} fr}{Gb^2}} - \frac{3f}{2\pi}. \quad (2)$$

In the derivation of Eqs. (1) and (2), the dislocation line tension is approximately taken as $Gb^2/2$.

Eqs. (1) and (2) indicate that the degree of hardening is $r^{1/2}$ dependence for the weak-coupling mechanism and inversely proportional to r for the strong-coupling mechanism. The hardening attributed to particle cutting is maximized at a critical precipitate radius r_{w} taking $\tau_{\text{weak}}^{\text{cutting}} = \tau_{\text{strong}}^{\text{cutting}}$. For the β′ phase in Mg-RE alloys, $\gamma_{\text{APB}} = 210$ mJ/m^2, $b = 0.32$ nm [44], $G = 16.5$ GPa [45], and $f = 0.12$ from Fig. 5d. Then the critical size r_{w}, corresponding to the transition between the weak- and strong-coupling mechanisms, is calculated to be 7.87 nm.

The CRSS for the Orowan looping mechanism is $\tau^{\text{Orowan}} = 3Gb/(2L_{\text{s}})$ with the mean precipitate spacing $L_{\text{s}} = r[2\pi/(3f)]^{1/2}$ [40,41]. Taking $\tau_{\text{strong}}^{\text{cutting}} = \tau^{\text{Orowan}}$, the critical precipitate size r_{c} corresponding to the mechanism transition from the particle cutting to Orowan looping is

$$r_{\text{c}} = \frac{Gb^2(4 + 9\pi^2)}{8\pi\gamma_{\text{APB}}}. \quad (3)$$

For the β′ phase in Mg-RE alloys, $r_{\text{c}} = 29.7$ nm from Eq. (3). Note that Eq. (3) is derived assuming spherical precipitates. For the triangular arrayed prismatic β′ precipitate plates, the effective planar inter-particle spacing is $L_{\text{p}} = 1.65[d_{\text{p}}t_{\text{p}}/(\pi f)]^{1/2} - 1.572d_{\text{p}}/\pi - 0.866t_{\text{p}}$ [20]. Taking $L_{\text{p}} = L_{\text{s}}$, an equivalent radius r_{eq} of the larger β′ precipitates in the BDF+250 °C × 12 h samples is estimated to be around 6.18 nm. Both the maximum precipitate radius $r_{\text{max}} = 2.5$ nm in the BDFed samples (Fig. 5d,f) and the equivalent planar radius $r_{\text{eq}} = 6.18$ nm of the larger precipitates in the BDF+250 °C × 12 h samples are significantly smaller than the critical precipitate size $r_{\text{c}} = 29.7$ nm from Eq. (3), indicating that the precipitates in both BDF samples and BDF+250 °C × 12 h samples are responsible for strengthening owing to the particle cutting mechanism. The particle cutting mechanism for the larger precipitates in the BDF+250 °C × 12 h samples is consistent with the TEM observation of the ordered prismatic plate-shaped β′ precipitates sheared by the basal slip of <a> dislocations in Mg alloy WE43 [44]. Since $r_{\text{eq}} = 6.18$ nm of the larger precipitates and the critical size $r_{\text{w}} = 7.87$ nm corresponding to the transition between the weak- and strong-couplings are about the same size, 12 hours can be regarded as an optimized time for the BDFed GW113 samples at 250 °C to fully harness precipitate strengthening.

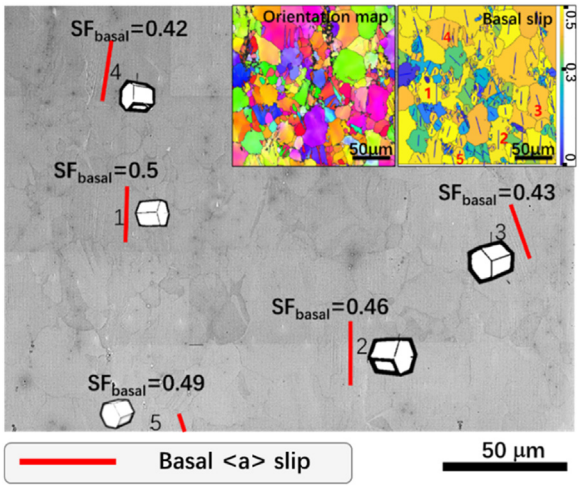

Fig. 13. Slip traces analysis of the PFD sample. Insets are the corresponding orientation map and basal slip Schmid factor map determined using MTEX. Blue lines in the basal slip map denote the theoretical slip traces of basal <a> slip.

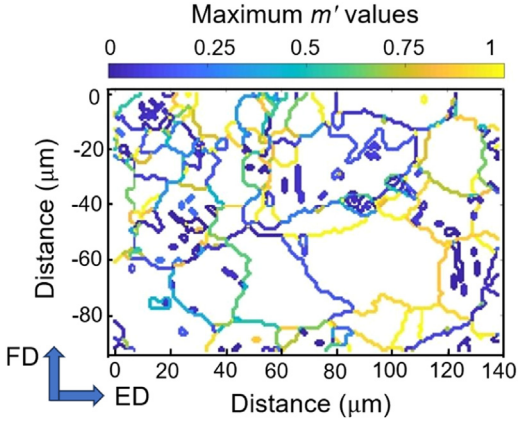

Fig. 14. A distribution diagram of the maximum value of the strain coordination factor m' of part of GBs in Fig. 6 when only basal slip is activated. Tensile loading is along FD.

In addition to the strengthening mechanisms discussed above, other factors can also influence mechanical properties of the high-strength alloys. For instance, recent studies indicate that introducing $\{10\bar{1}2\}$ twins can have a similar

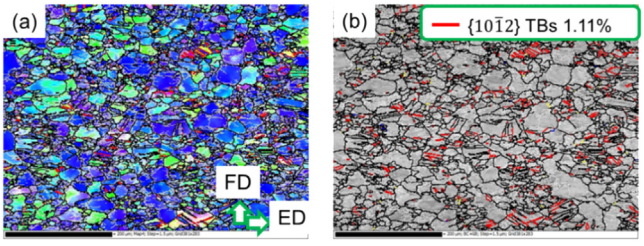

Fig. 15. IPF colored orientation map (a) and IQ image supervised with TBs (b) of the PED sample after tension to failure. Scale bars, 200 μm.

impact on strength as grain refinement [46]. However, for the BDFed GW113 alloy studied in the current work, TB refinement only contributes 3 MPa to the yield strength according to the Hall–Petch relation. This suggests that the twinning strengthening effect is limited here.

4.2. Mechanism underlying the impact of texture on ductility anisotropy in the BDFed sample

As texture has a significant impact on the mechanical properties of alloys, it can exacerbate or mitigate the commonly observed strength-ductility paradox in metallic alloys [12]. To better understand the mechanism underlying the influence of texture on the mechanical anisotropy and strength–ductility synergy of BDFed GW113 alloy in ED, we perform slip trace analysis on a randomly selected region of both PED and PFD samples after tensile failure.

Fig. 13 shows the slip trace analysis of the PFD sample deformed to failure. The region of around 200 μm × 200 μm in the gauge is randomly selected. Due to the low ductility, only five grains show visible slip traces, which shall be the basal <a> slip in comparison with the theoretical basal <a> slip traces (right inset in Fig. 13). It is shown that the basal <a> slip is the dominant plastic deformation mechanism of the PFD sample and the grains with the activated basal <a> slip have high Schmid factor (SF_{basal}) values (≥0.42). For the PFD sample, the texture promotes basal slip with high Schmid factor values. Therefore, it was thought that the low yield strength of PFD sample related to the texture as basal slip can occur in many grains even under low stress conditions.

The strain coordination factor m' distribution map of the BDFed alloy (Fig. 14) shows that when only basal plane slip is activated, the intergranular coordination factor m' of the PFD sample tends to be low. This suggests that coordinating plastic deformation between adjacent grains becomes difficult when the basal slip is simultaneously activated in the PFD sample. Therefore, the texture-induced basal slip, as the dominant plastic deformation mechanism, also contributes to the low ductility of the PFD sample.

In contrast, the texture leads to high elongation of the PED sample while hindering the basal slip and improving the yield strength. Previous studies have suggested that the increase in ductility caused by texture may be due to the reduction of the anisotropy of activation stresses of basal <a> and non-basal slip systems [47]. The twinning deformation mechanism is excluded, since there is not much difference in grain size and

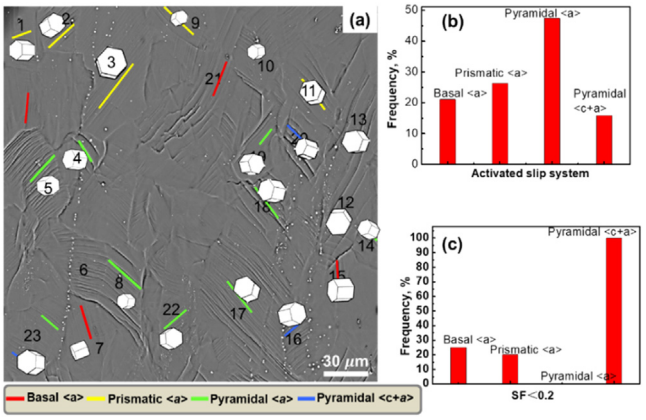

Fig. 16. Slip traces (a) and frequencies of different activated slip systems (a) and these with Schmid factor (SF) lower than 0.2 in the PED sample upon tensile loading to failure.

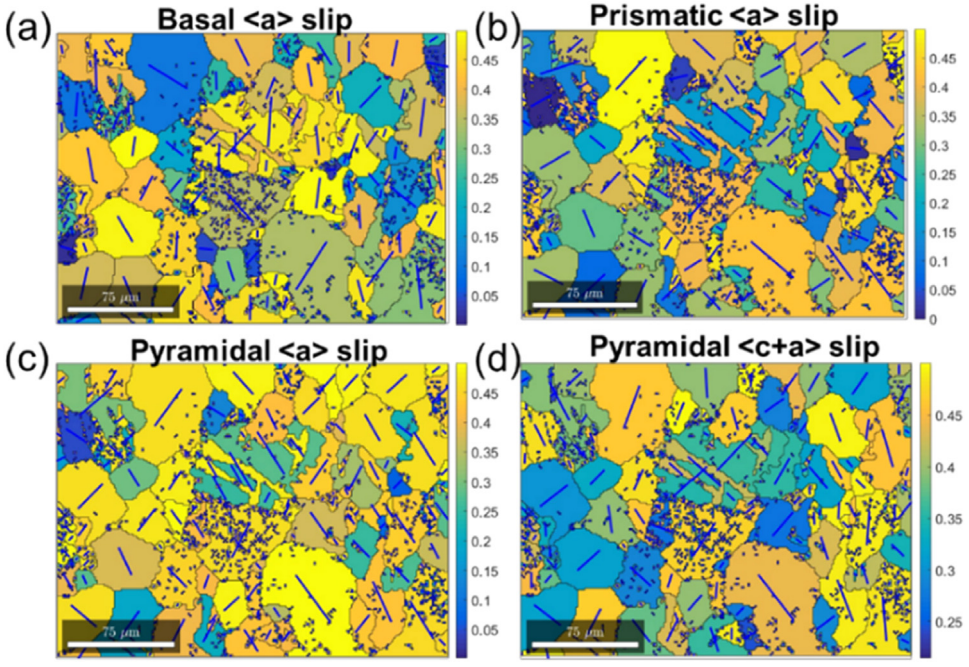

Fig. 17. The Schmid factor maps of Fig. 16 determined using MTEX. Blue lines denote the theoretical slip traces of (a) basal <a> slip, (b) prismatic <a> slip ({1-100} plane) (c) pyramidal <a> slip ({1-101}plane) and (d) pyramidal <c + a> slip ({11-22}plane). Scale bars, 75 μm.

Table 2
The average non-basal slip Schmid factors of the BDFed GW113 alloy in Fig. 6 when loaded along ED, FD (x), and FD (y).

Average Schmid factors		Slip systems		
		Prismatic <a>	Pyramidal <a>	Pyramidal <c + a>
Tensile directions	ED	0.45	0.45	0.43
	FD (x)	0.26	0.36	0.37
	FD (y)	0.25	0.35	0.37

the type, morphology, and volume fractions of twins in the PED sample before and after tension (Figs. 6 and 15). This observation suggests that twinning is not the dominant plastic deformation during the tension of the PED sample. Notably, a slight reduction in the number of the twin boundaries (TBs) observed in Fig. 15 could be due to the easy migration of the $\{10\bar{1}2\}$ TBs [48]. Overall, the high elongation in the PED sample can be attributed to many factors including reduced anisotropy of activation stresses, hindered basal slip, and enhanced yield strength due to texture.

Fig. 16 presents the slip trace analysis and their statistical results of around 23 grains in the PED sample. The slip traces in Fig. 16a are identified by comparison with theoretical slip traces of different slip systems (Fig. 17). The plastic deformation mechanism in the PED sample contains basal <a> slip, prismatic <a> slip, pyramidal <a> slip and pyramidal <c + a> slip (Fig. 16). The abundant slip activities are responsible for the high ductility of the PED sample. The statistical results show that pyramidal <a> slip accounts for approximately 48% of slip activity (Fig. 16b), making it the slip system with the highest occurrence frequency. Fig. 16c shows that the occurrence of pyramidal <a> slip traces do not exhibit the non-Schmid effect, indicating that this plastic deformation is easily activated due to the high Schmid factor (Fig. 16c).

The high activity of non-basal slip in GW103 and WGZ1152 alloys is observed owing to the presence of high rare-earth content [49–51]. However, for the present BDFed GW113 alloy with high rare-earth content, the non-basal slip traces only prevail when the alloy is deformed along ED (i.e., PED sample) but not along FD(x/y) (i.e., PFD sample) (Figs. 13 and 16). This observation suggests that the activation of the non-basal slip in the PED sample should be related to its particular texture since the main difference between the PED and the PFD samples is the texture-induced Schmid factor difference. For the PED samples, the Schmid factors of the basal slip induced by the texture are of a relatively low average value (0.16) (Fig. 11) and the average value of the non-basal slip Schmid factors is relatively high 0.43∼0.45 (Table 2). As a contrast, the average Schmid factor values of the three typical non-basal slip systems in the PFD sample are much lower (0.25∼0.37). Therefore, it can be concluded that the pyramidal slip system overcomes the basal slip system with the lowest CRSS and becomes the most activated slip system, mainly due to the texture effect leading to a higher *m*-value for the pyramidal slip system and a lower *m*-value for the basal slip system.

Note that the high ductility of the PED sample is not only due to the occurrence of the pyramidal <a> slip but also associated with the appearance of pyramidal <c + a> slip which can provide five independent slip systems. Fig. 16c shows that the pyramidal <c + a> slip has non-Schmid effect, which is probably associated with the local-stress fluctuation near GB caused by strain accommodation between grains [52]. Therefore, the non-Schmid effect of pyramidal <c + a> slip indicates that the critical shear stress of pyramidal <c + a> slip is high and its occurrence needs high stress concentrations at GBs. Because the activation of the <c + a> slip on the pyramidal planes is difficult, only a few <c + a> slips are identified from the slip traces (Fig. 16). As the slip trace method has a risk of mislabeling, the dislocation types of the PED sample before and after stretching are further analyzed using TEM double beam diffraction to verify the small amount of pyramidal

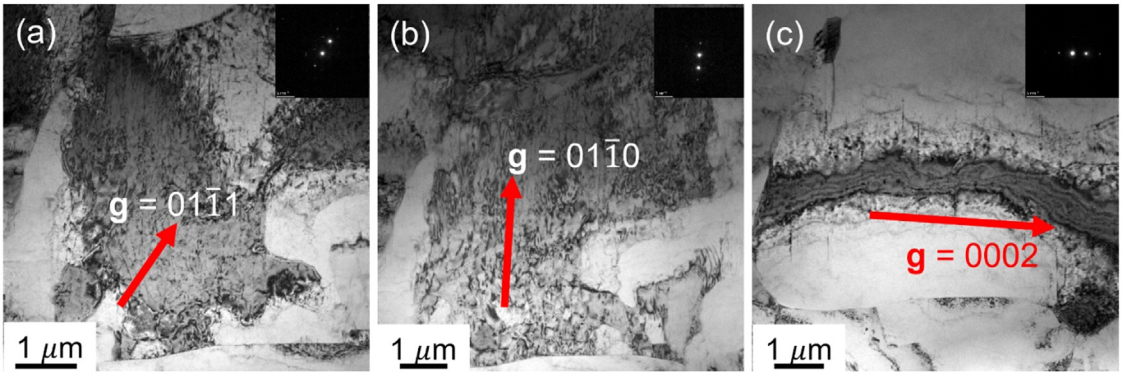

Fig. 18. Bright-field images of dislocations in the PED sample before tension. Images are taken at the same region but with different diffraction conditions.

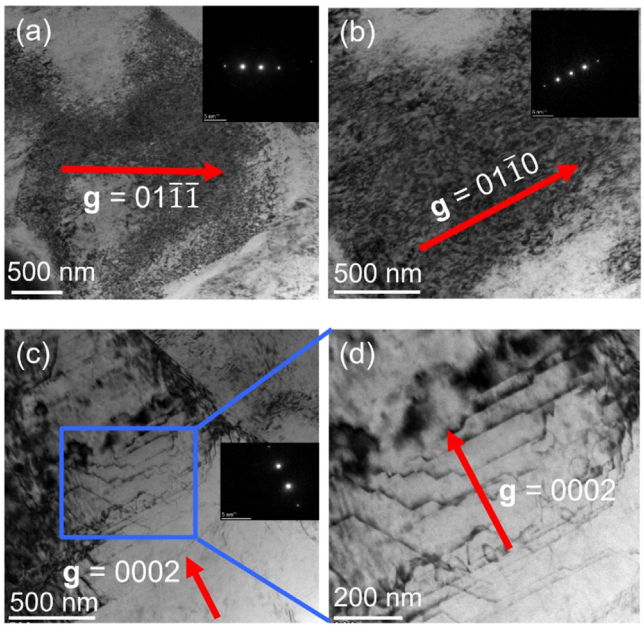

Fig. 19. Bright-field images of dislocations in the PED sample upon tensile loading to failure. Images are taken at the same region but with different diffraction conditions. (d) Magnified view of the block in (c).

<c + a> slip activities. Fig. 18 indicates that the initial dislocations in the PED sample before tension are dominant <a> type that can be observed along the diffraction vector $\mathbf{g} = [01\bar{1}1]$ and $\mathbf{g} = [01\bar{1}0]$ but not along $\mathbf{g} = [0002]$. Upon tension, dislocation cells are observed along $\mathbf{g} = [01\bar{1}1]$ and $\mathbf{g} = [01\bar{1}0]$ (Fig. 19a,b) while they appear as clear dislocation lines observing along $\mathbf{g} = [0002]$ (Fig. 19c,d). Figs. 18 and 19 together indicate that the pyramidal <c + a> slip occurs during the tension of the PED sample.

The preceding discussion indicates that texture plays a crucial role in determining the mechanical properties of the BDFed GW113 alloy. Specifically, the basal texture featuring two peaks tilted approximately 39° from FD (x) to FD (y) is responsible for enhancing both strength and ductility in ED while creating strength and ductility anisotropies in ED and FD.

5. Conclusions

In this work, we propose a novel bi-directional forging (BDF) process which enables the fabrication of high-strength Mg-11Gd-3Y-0.5Zr (GW113) alloy in an efficient and low-cost manner compared with multi-directional forging processes. Upon a total compressive strain of 1.83 during forging the GW113 alloy in the as-homogenized state, the PED sample, with axial direction parallel to the elongation direction, exhibits significantly improved tensile strength (from 174 MPa to 312 MPa) and ductility (from 3.7% to 14.5%) along the tensile loading direction. Moreover, the annealed PED sample exhibits an ultra-high yield strength of 474 MPa, higher than that of most magnesium alloys reported in literature. In contrast, the PFD sample, with axial direction parallel to the forging direction, has strength and ductility of similar values to those of the GW113 alloy in the initial as-homogenized state.

The deformation mechanisms are analyzed at both intragranular and intergranular levels. It is revealed that texture weakening in the PFD sample counteracts grain refinement strengthening and precipitate strengthening. In contrast, texture leads to the simultaneous improvement of strength and ductility of the PED sample. This is attributed to the reduction in anisotropy of basal slip and non-basal slip, which significantly improves the yield strength of the PED samples and promotes the activation of the non-basal slip system, including pyramidal <c + a> slip. It is further revealed that pyramidal <c + a> slip plays a crucial role in plastic deformation and strain coordination between grains, serving as the main reason for the high elongation of the PED samples.

Declaration of competing interest

The authors have no conflicts of interest to disclose.

CRediT authorship contribution statement

Jingli Li: Writing – original draft, Methodology, Investigation, Funding acquisition, Formal analysis, Conceptualization. **Quanfeng Han:** Methodology, Investigation, Formal analysis. **Xiuzhu Han:** Investigation. **Xin Yi:** Writing – review & editing, Project administration, Methodology, Investigation, Funding acquisition, Formal analysis, Conceptualization.

Acknowledgments

This work is supported by the National Natural Science Foundation of China (11988102 and 52301146), Chinese Postdoctoral Science Foundation (8206300226), National Science and Technology Infrastructure Platform Development Plan-Young Backbone Talents Training Project (52001325) and the Fundamental Research Funds for the Central Universities (JB2023118).

References

[1] H. Yu, Y. Xin, M. Wang, Q. Liu, J. Mater. Sci. Technol. 34 (2018) 248–256.
[2] R.Z. Valiev, T.G. Langdon, Prog. Mater. Sci. 51 (2006) 881–981.
[3] T. Peng, Q. Wang, J. Lin, M. Liu, H.J. Roven, Mater. Sci. Eng. A 528 (2011) 1143–1148.
[4] J. Lin, X. Wang, W. Ren, X. Yang, Q. Wang, J. Mater. Sci. Technol. 32 (2016) 783–789.
[5] J. Zhao, H. Guo, T. Luo, C. Zhang, J. Luo, J. Alloys Compd. 928 (2022) 167199.
[6] A. Sheikhani, R. Roumina, R. Mahmudi, J. Mater. Res. Technol. 18 (2022) 4089–4098.
[7] W.J. Kim, S.I. Hong, Y.S. Kim, S.H. Min, H.T. Jeong, J.D. Lee, Acta Mater. 51 (2003) 3293–3307.
[8] T. Mukai, M. Yamanoi, H. Watanabe, K. Higashi, Scr. Mater. 45 (2001) 89–94.
[9] J. Lin, W. Ren, Q. Wang, L. Ma, Y. Chen, Adv. Mater. Sci. Eng. 2014 (2014) 356572.

[10] L.B. Tong, J.H. Chu, W.T. Sun, C. Xu, D.N. Zou, K.S. Wang, M.Y. Zheng, Mater. Charact. 171 (2021) 110804.
[11] G. Garces, P. Pérez, R. Barea, J. Medina, A. Stark, N. Schell, P. Adeva, Metals 9 (2019) 221.
[12] Q. Han, J. Li, X. Yi, J. Mech. Phys. Solids 173 (2023) 105200.
[13] M. Hong, D. Wu, R.S. Chen, X.H. Du, J. Magnes. Alloys 2 (2014) 317–324.
[14] S.S.A. Shah, D. Wu, W.H. Wang, R.S. Chen, Mater. Sci. Eng. A 702 (2017) 153–160.
[15] M. Ahmadi, B. Salgın, M. Ahmadi, B.J. Kooi, Y. Pei, Int. J. Plast. 144 (2021) 103041.
[16] D. Mercier, C. Zambaldi, T.R. Bieler, IOP Conf. Ser.: Mater. Sci. Eng. 82 (2015) 012090.
[17] J. Sun, L. Jin, J. Dong, F. Wang, S. Dong, W. Ding, A.A. Luo, Int. J. Plast. 123 (2019) 121–132.
[18] J. Li, N. Zhang, X.X. Wang, D. Wu, R.S. Chen, Acta Metall. Sin. 31 (2018) 189–198.
[19] J. Li, Z. Dong, X. Yi, D. Wu, R. Chen, J. Magnes. Alloys 11 (2023) 2285–2298.
[20] J.F. Nie, Scr. Mater. 48 (2003) 1009–1015.
[21] Y. Yuan, X. Li, W. Yang, J. Mech. Phys. Solids 130 (2019) 280–296.
[22] H. Wang, C.J. Boehlert, Q.D. Wang, D.D. Yin, W.J. Ding, Int. J. Plast. 84 (2016) 255–276.
[23] Y. Wang, Y. Xin, A. Chapuis, H. Yu, Q. Liu, Metall. Mater. Trans. A 47 (2016) 4276–4286.
[24] J. Li, D. Wu, R. Chen, E. Han, JOM 71 (2019) 2010–2017.
[25] W. Liu, B. Zhou, G. Wu, L. Zhang, X. Peng, L. Cao, J. Magnes. Alloys 7 (2019) 597–604.
[26] K.Y. Zheng, J. Dong, X.Q. Zeng, W.J. Ding, Mater. Sci. Eng. A 454-455 (2007) 314–321.
[27] S.K. Panigrahi, W. Yuan, R.S. Mishra, R. DeLorme, B. Davis, R.A. Howell, K. Cho, Mater. Sci. Eng. A 530 (2011) 28–35.
[28] Y.B. Hu, J. Deng, C. Zhao, F.S. Pan, J. Peng, J. Mater. Sci. 46 (2011) 5838–5846.
[29] X. Liu, W. Hu, Q. Le, Z. Zhang, L. Bao, J. Cui, Mater. Sci. Eng. A 612 (2014) 380–386.
[30] M. Hong, S.S.A. Shah, D. Wu, R.S. Chen, X.H. Du, N.T. Hu, Y.F. Zhang, Met. Mater. Int. 22 (2016) 1091–1097.
[31] S. You, Y. Huang, K.U. Kainer, N. Hort, J. Magnes. Alloys 5 (2017) 239–253.
[32] Y. Estrin, A. Vinogradov, Acta Mater. 61 (2013) 782–817.
[33] R.G. Li, J.F. Nie, G.J. Huang, Y.C. Xin, Q. Liu, Scr. Mater. 64 (2011) 950–953.
[34] X. Li, C. Liu, T. Al-Samman, Mater. Lett. 65 (2011) 1726–1729.
[35] Q. Wei, L. Yuan, X. Ma, M. Zheng, D. Shan, B. Guo, Mater. Sci. Eng. A 831 (2022) 142144.
[36] X. Xu, X. Chen, W. Du, Y. Geng, F. Pan, Mater. Sci. Technol. 33 (2017) 926–934.
[37] Y. Wang, H. Choo, Acta Mater. 81 (2014) 83–97.
[38] Q. Han, X. Yi, J. Mech. Phys. Solids 154 (2021) 104530.
[39] Q. Han, X. Yi, Int. J. Plast. 153 (2022) 103261.
[40] E. Orowan, In: Symposium on Internal Stresses in Metals and Alloys. The Institute of Metals, London, 1948, pp. 451–453.
[41] B. Reppich, In: Plastic Deformation and Fracture of Materials (H. Mughrabi Ed.), Materials Science and Technology (R.W. Cahn, P. Haasen, E.J. Kramer Eds.), Vol. 6. Wiley-VCH, Weinheim, 1996.
[42] R.C. Reed, The Superalloys: Fundamentals and Applications, Cambridge University Press, Cambridge, 2006.
[43] Q. Fang, L. Li, J. Li, H. Wu, Z. Huang, B. Liu, Y. Liu, P.K. Liaw, J. Mech. Phys. Solids 122 (2019) 177–189.
[44] J.J. Bhattacharyya, F. Wang, N. Stanford, S.R. Agnew, Acta Mater. 146 (2018) 55–62.
[45] S.M. He, X.Q. Zeng, L.M. Peng, X. Gao, J.F. Nie, W.J. Ding, J. Alloys Compd. 427 (2007) 316–323.
[46] S.G. Hong, S.H. Park, C.S. Lee, Acta Mater. 58 (2010) 5873–5885.
[47] S.R. Agnew, Ö. Duygulu, Int. J. Plast. 21 (2005) 1161–1193.
[48] H. Su, X. Zhou, S. Zheng, H. Ye, Z. Yang, Scr. Mater. 206 (2022) 114237.
[49] D.D. Yin, C.J. Boehlert, L.J. Long, G.H. Huang, H. Zhou, J. Zheng, Q.D. Wang, Int. J. Plast. 136 (2021) 102878.
[50] R. Ni, Z.W. Jiang, D.D. Yin, W. Yang, H. Zhou, J. Zheng, Q.D. Wang, Metall. Mater. Trans. A 53 (2022) 535–555.
[51] R. Ni, S.J. Ma, L.J. Long, J. Zheng, H. Zhou, Q.D. Wang, D.D. Yin, Mater. Sci. Eng. A 804 (2021) 140738.
[52] C. Lou, X. Zhang, Y. Ren, Mater. Charact. 107 (2015) 249–254.